

Phil Preikschas, Milivoj Plodinec, Julia Bauer, Ralph Kraehnert, Raoul Naumann d'Alnoncourt, Robert Schlögl, Matthias Driess, Frank Rosowski

Tuning the Rh–FeOx interface in ethanol synthesis through formation phase studies at high pressures of synthesis gas

Open Access via institutional repository of Technische Universität Berlin

Document type

Journal article | Accepted version

(i. e. final author-created version that incorporates referee comments and is the version accepted for publication; also known as: Author's Accepted Manuscript (AAM), Final Draft, Postprint)

This version is available at

<https://doi.org/10.10.14279/depositonce-16078>

Citation details

Preikschas, P., Plodinec, M., Bauer, J., Kraehnert, R., Naumann d'Alnoncourt, R., Schlögl, R., Driess, M., & Rosowski, F. (2021). Tuning the Rh–FeOx Interface in Ethanol Synthesis through Formation Phase Studies at High Pressures of Synthesis Gas. In ACS Catalysis (Vol. 11, Issue 7, pp. 4047–4060). American Chemical Society (ACS). <https://doi.org/10.1021/acscatal.0c05365>.

This document is the Accepted Manuscript version of a Published Work that appeared in final form in ACS Catalysis, copyright © 2021 The Authors after peer review and technical editing by the publisher. To access the final edited and published work see <https://doi.org/10.1021/acscatal.0c05365>.

Terms of use

This work is protected by copyright and/or related rights. You are free to use this work in any way permitted by the copyright and related rights legislation that applies to your usage. For other uses, you must obtain permission from the rights-holder(s).

Tuning the Rh-FeO_x Interface in Ethanol Synthesis through Formation Phase Studies at High Pressures of Synthesis Gas

Phil Preikschas,[†] Milivoj Plodinec,[‡] Julia Bauer,[†] Ralph Kraehnert,[†]

Raoul Naumann d'Alnoncourt,^{†} Robert Schlögl,^{†,‡} Matthias Driess,^{†,§} and Frank Rosowski^{†,||}*

[†]BasCat, UniCat BASF JointLab, Technische Universität Berlin, Hardenbergstraße 36, Sekr.
EW-K01, 10623 Berlin

[‡]Department of Inorganic Chemistry, Fritz-Haber-Institut der Max-Planck-Gesellschaft,
Faradayweg 4-6, 14195 Berlin

[§]Metalorganic Chemistry and Inorganic Materials, Department of Chemistry, Technische
Universität Berlin, Straße des 17. Juni 135, Sekr. C2, 10623 Berlin

^{||}BASF SE, Process Research and Chemical Engineering, Heterogeneous Catalysis, Carl-Bosch-
Straße 38, 67056 Ludwigshafen

ABSTRACT

As-prepared materials tested for a catalytic reaction are usually only pre-catalysts that become active and/or selective under specific conditions. During this initial formation phase, catalysts can undergo a change in their structure, morphology, chemical state, or even composition. This dynamic behavior has a vital impact on reactivity, and we identified that this initial formation phase is also critical for Rh in the catalytic conversion of synthesis gas to oxygenates and ethanol in particular. The syngas-to-ethanol reaction (StE) is a promising alternative route to ethanol from fossil and non-fossil carbon resources. Despite heavy research efforts, rates and selectivities still need to be improved for industrial operations. For this reason, structure-function relationships at industrially relevant reaction conditions must be clarified. Although some *in situ* and *operando* studies have been reported, a pressure gap still exists between experimental and process-relevant high-pressure conditions. To overcome this pressure gap and investigate the dynamic behavior of Rh-based catalysts under reaction conditions, we applied a generic method for formation phase studies at high partial pressures of synthesis gas where standard *operando* methods are inapplicable. Combining integral and local characterization methods before and after a long-term catalytic test of a RhFeO_x/SiO₂ catalyst (>140 h on stream) allowed us to ascribe a drastic decrease in ethanol formation to a structural change from an unalloyed RhFeO_x to an alloyed RhFe/FeO_x nanostructure. Our investigation provides an explanation for the great variation of reported catalytic results of RhFe catalysts and their nanostructures in synthesis gas conversion. The structure-function relationship we identified finally provides the opportunity for improved catalyst design strategies: stabilizing the Rh-FeO_x interface by preventing RhFe nanoalloy formation. As one example, we report a RhFeO_x catalyst on a high surface area Mn₂O₃ support which decreases the Fe mobility and reducibility through the formation of a (Fe,Mn)O_x mixed surface oxide.

Stabilizing the Rh-FeO_x interface finally led to stable ethanol selectivity, and the formation of RhFe nanoalloy structures was not observed.

KEYWORDS: CO hydrogenation, rhodium, iron, nanoalloy, ethanol, synthesis gas

INTRODUCTION

Heterogeneous catalysts often change their properties during chemical transformations under common reaction conditions such as medium to high temperatures and elevated pressures. This change in catalyst structure, morphology, composition, and chemical state affects their reactivity and stability over time.¹⁻³ Knowledge of catalytic behavior under process-relevant conditions is not only crucial for a fundamental understanding of promoter effects and reaction mechanisms, it is also important for estimating catalyst lifetime, which in turn is key to operating industrial-scale facilities in a resource- and cost-efficient manner.⁴ In this context, predicting and designing an efficient catalyst is not possible when considering peak performance marks only. Long-term catalytic tests need to identify changes encountered in the stability and reactivity of catalysts. Neglecting this crucial aspect might lead to converse or incomparable catalytic results for similar catalyst systems, e.g., significant variation in selectivity patterns of pure Rh/SiO₂ catalysts in CO hydrogenation.⁵

One way to overcome these issues are *in situ* and/or *operando* experiments, which often provide desired insights into the properties of working catalysts under relevant conditions, such as identification of titled carbonyl species on Rh/SiO₂ samples that are probable precursors for hydrogen-assisted CO dissociation in the conversion of synthesis gas to oxygenates.⁶ However, those *in situ* or *operando* investigations can be challenging when a process under high pressures is studied, and a pressure gap still exists between experimental and industrially relevant conditions.⁷ Specifically, spectroscopic investigations are difficult at high CO partial pressures as gas-phase CO interferes with adsorbed carbonyl species. Common workarounds to minimize the void volume require cell designs that prohibit homogeneous heat and mass distribution within the cell.⁷⁻¹⁰ As a consequence, many reported *in situ* studies were performed under ambient pressure

conditions. Conclusions drawn from those studies should be regarded with caution when correlated with catalyst reactivity under high pressure reaction conditions.

When *in situ* or *operando* investigations are inaccessible or inapplicable, the detailed characterization of a catalytic material prior to and after catalytic reaction can yield meaningful information as reported for the deactivation of Pd catalysts through the disintegration of particles into single atoms.¹¹ In this case, it is apparent that the materials investigated need to be activated under the same conditions as in the catalytic process since the as-prepared materials are usually only pre-catalysts that become active under these specific conditions.⁴ Moreover, all catalysts have to be handled under a protective atmosphere or, in the case of as-prepared materials, should be activated *in situ* prior to characterization.

For example, syngas (CO/H₂) conversion reactions are often difficult to investigate with *in situ* and *operando* techniques because the applied reaction conditions usually involve high pressures and atmospheres with high CO content.⁷ However, syngas as alternative feedstock for the production of base chemicals is becoming increasingly interesting in light of growing climate and carbon management concerns. The production of ethanol is a good example of this transition. To date, ethanol is produced primarily by fermentation from corn or sugarcane. However, growing demand for synthetic ethanol as a fuel or fuel additive requires alternative, more scalable production routes.

The direct synthesis of ethanol from synthesis gas has been studied extensively but ethanol yields still need to be improved for industrial application.¹²⁻¹⁴ As Rh-based catalysts have shown the most promising results, several promoter screenings were conducted in which Fe, Mn, and Li were shown to be the most-effective.¹² Accordingly, supported Rh(Mn,Fe)O_x materials rank among the best catalysts in terms of ethanol yield in CO hydrogenation. Although a wide range of catalysts

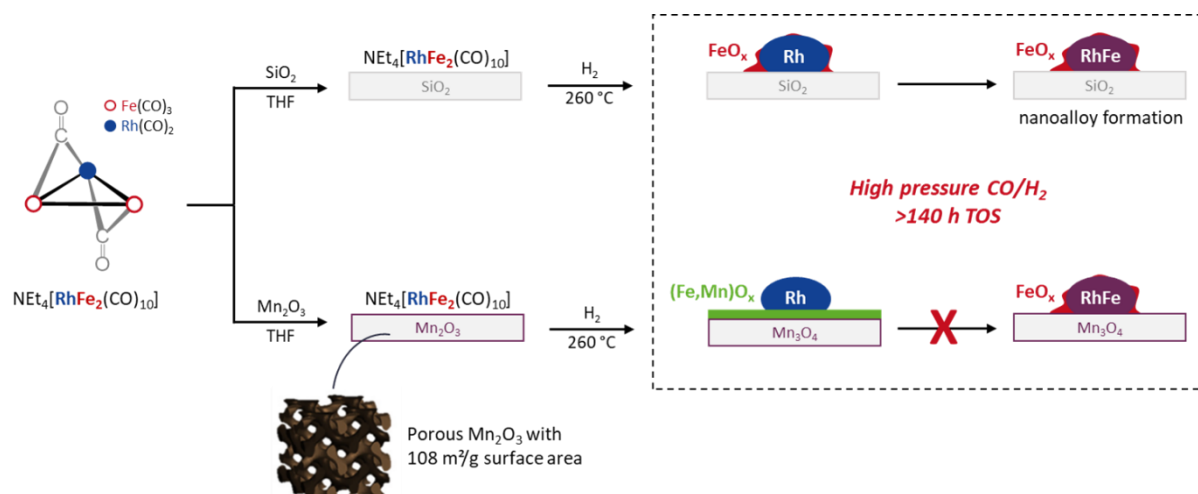
has been tested, the intrinsic reaction mechanism is still elusive and the role of promoters is unclear due to the complexity of the multi-promoted catalyst systems and the above-mentioned inapplicability of standard *operando* methods.^{15–17} To combat this complexity and further improve these multi-promoted Rh-based catalysts, an in-depth understanding of the respective single-promoted RhMnO_x and RhFeO_x systems is needed.

In case of single-promoted RhMnO_x systems, it is widely accepted that the superior reactivity is based on close proximity between Rh and MnO_x through strong metal-promoter interactions.^{12,18–20} Although the formation of a RhMn nanoalloy structure was initially proposed, the actual nanostructure of RhMnO_x catalysts has been found to consist of metallic Rh particles decorated with an amorphous MnO_x phase.²⁰ Furthermore, we demonstrated in a previous publication that not even the use of Na₂[Rh₃Mn₃(CO)₁₈] as a molecular precursor with both metals in low oxidation states and predefined metal-metal bonds led to the formation of a RhMn nanoalloy.²¹

In contrast, the nanostructure of RhFeO_x catalysts is still under debate and the proposed structural models vary from unalloyed RhFeO_x over core-shell to nanoalloyed RhFe structures.^{6,22–30} Likewise, the formation of oxygenate products varies significantly on similar catalyst systems, resulting in reported methanol selectivities ranging from 0–13.5 % and ethanol selectivities from 8–35 %. According to Haider and co-workers, the addition of Fe leads to an increased selectivity towards ethanol by stabilizing Rh⁺(CO)₂ sites on unalloyed RhFeO_x catalysts, which promotes CO insertion.²² In contrast, Hartman *et al.* stated that RhFe nanoalloyed structures reduce tilted carbonyl species at the surface, thus enhancing CO insertion and selectivity towards ethanol.⁶ However, Mo and co-workers ascribe higher selectivities towards methane and methanol to the modification of Rh-based catalysts with Fe and only a small improvement in EtOH selectivity was observed.²⁸ Although several structural models have been proposed, a systematic investigation of

the impact of time on stream under relevant reaction conditions has not been performed to the best of our knowledge.

Herein, we report a generic method for formation phase studies at high partial pressure of synthesis gas. We identified this formation phase to be critical for the conversion of synthesis gas to ethanol and observed a significant change in oxygenate selectivity. Combining integral and local characterization methods before and after this long-term catalytic study (>140 h on stream) allowed us to ascribe this dynamic behavior to a structural change from an unalloyed Rh–FeO_x to an alloyed RhFe/FeO_x nanostructure (Scheme 1, top). In this study, we propose an explanation for the great variation of reported catalytic results of Fe-promoted Rh catalysts in CO hydrogenation. The structure-function relationship we identified finally provides the opportunity for improved catalyst design strategies. As one example, we report a RhFeO_x catalyst on a novel high surface area Mn₂O₃ support³¹ which prevents RhFe alloying through formation of a (Fe,Mn)O_x mixed surface oxide (Scheme 1, bottom).



Scheme 1. Synthesis of RhFeO_x model catalysts over a single-source precursor approach: using $\text{NEt}_4[\text{RhFe}_2(\text{CO})_{10}]$ as single-source precursor (SSP) leads to a well-defined, unalloyed $\text{RhFeO}_x/\text{SiO}_2$ model catalyst (top). During the critical formation phase in CO hydrogenation, the catalyst undergoes a structural transformation from an unalloyed RhFeO_x to an alloyed RhFe/FeO_x nanostructure accompanied by a significant change in oxygenate selectivity. The same SSP approach on a high surface area Mn_2O_3 support leads to a $\text{Rh}/(\text{Fe,Mn})\text{O}_x$ catalyst (bottom). The formation of $(\text{Fe,Mn})\text{O}_x$ mixed surface oxides prevents RhFe nanoalloy formation.

EXPERIMENTAL SECTION

General considerations. All manipulations involving air and moisture sensitive organometallic compounds were carried out under an atmosphere of dry, oxygen-free argon by using standard Schlenk techniques or glove boxes (MBraun LABmaster Pro) under a purified nitrogen or argon atmosphere. The solvents were taken from a solvent purification system (MBraun SPS-800) or purified using conventional procedures, freshly distilled under argon atmosphere, and degassed prior to use. NMR spectra were recorded on a Bruker AvanceIII (1H: 700 MHz, 13C: 125 MHz) spectrometer and referenced to residual solvent signal as internal standards (tetrahydrofuran-*d*₈: δ H = 1.72 ppm, δ C = 25.3 ppm). IR spectrum was recorded on a Nicolet iS5 spectrometer inside a glove box. Mass spectrum was recorded using HR-ESI-MS-method on a LTQ Orbitrap XL spectrometer. The mass fractions of C, H, N, and S were determined on a Thermo Finnigan FlashEA 1112 Organic Elemental Analyzer. The starting material $\text{NEt}_4[\text{FeH}(\text{CO})_4]$ was synthesized according to a known literature procedure.³² SiO_2 (Davisil grade 635) was preheated at 100 °C under vacuum overnight before use. All other reagents were used as received.

Synthesis of $\text{NEt}_4[\text{RhFe}_2(\text{CO})_{10}]$. $\text{NEt}_4[\text{FeH}(\text{CO})_4]$ (3.27 g, 10.9 mmol) was dissolved in 30 mL tetrahydrofuran (THF) and a solution of $[\text{Rh}(\text{CO})_2\text{Cl}]_2$ (1.23 g, 3.18 mmol) in THF (40 mL) was added dropwise. Stirring at r.t. overnight resulted in the precipitation of a colorless solid. The residue was washed with addition of 20 mL THF, and the combined filtrates were evaporated under vacuum overnight leading to a black powder. Yield: 2.98 g, 4.77 mmol, 43.7 % (based on $\text{NEt}_4[\text{FeH}(\text{CO})_4]$). Elemental analysis (%): calcd. for $\text{C}_{18}\text{H}_{20}\text{NO}_{10}\text{Fe}_2\text{Rh}$: C, 34.6; H, 3.23; N, 2.24; found: C, 34.9; H, 3.55; N, 2.16. HR-ESI-MS (m/z): calcd. for $[\text{M}-\text{NEt}_4]$: 494.72, found: 494.73. ¹H NMR (700 MHz, THF-*d*₈, 298 K, ppm): δ = 1.35 (t, CH_3), 3.35 (q, CH_2). ¹³C{¹H} NMR (125

MHz, THF-*d*₈, 298 K, ppm): δ = 6.58 (s, CH₃), 52.1 (s, CH₂), 216 (m, CO). IR (ATR, cm⁻¹): ν = 2055 (m), 1994 (w), 1974 (m), 1908 (s), 1870 (s).

Synthesis of carbonyl-derived RhFeO_x/SiO₂. A solution of NEt₄[RhFe₂(CO)₁₀] (0.236 g, 0.377 mmol) in THF (3.63 mL) was added to 1.35 g SiO₂ under mixing with a spatula inside a glove box. The addition of the solution was conducted in three steps á 1.21 mL, which corresponds to the specific pore volume of the support (0.90 mL/g) according to the incipient wetness impregnation method. After each impregnation step, the silica-supported precursor was dried under high vacuum for 12 h at room temperature. The pre-catalyst was reduced by thermal treatment in flowing 10 % H₂/Ar (total flow 500 mL/min) at 260 °C (T ramp 10 K/min) for 2 h. The final RhFeO_x/SiO₂ catalyst was kept under an inert gas atmosphere prior to use. Metal loadings by ICP-OES (wt%): 2.53 Rh, 2.01 Fe. Elemental analysis after catalysis (wt%): 1.57 C, 0.48 H, 0.00 N.

Synthesis of carbonyl-derived Rh/(Fe,Mn)O_x. The Rh/(Fe,Mn)O_x was synthesized by a similar procedure as described for RhFeO_x/SiO₂. High surface area Mn₃O₄ (2.48 g) was impregnated with a solution of NEt₄[RhFe₂(CO)₁₀] (0.234 g, 0.374 mmol) in THF (3.63 mL). The pre-catalyst was reduced by thermal treatment in flowing 10 % H₂/Ar (total flow 500 mL/min) at 260 °C (T ramp 10 K/min) for 2 h. The final Rh/(Fe,Mn)O_x catalyst was kept under an inert gas atmosphere prior to use. Metal loadings by ICP-OES (wt%): 1.14 Rh, 1.04 Fe. Elemental analysis (wt%): before catalysis: 0.16 C, 0.18 H, 0.00 N; after catalysis: 1.53 C, 0.12 H, 0.00 N.

Synthesis of carbonyl-derived Rh/SiO₂ reference materials. A solution of Rh₄(CO)₁₂ (70.6 mg, 94.4 μ mol) in DCM (3.69 mL) was impregnated on SiO₂ (1.36 g). The pre-catalyst was activated by thermal treatment in flowing 10 % H₂/Ar (total flow 500 mL/min) at 260 °C (T ramp

10 K/min) for 2 h. The final Rh/SiO₂ catalyst was kept under an inert gas atmosphere prior to use. Metal loadings by ICP-OES (wt%): 2.11 Rh.

Synthesis of FeO_x/SiO₂ reference materials. An aqueous solution of iron(III) nitrate Fe(NO₃)₃ was impregnated on silica (pretreated at 550 °C in air for 6 h). A subsequent calcination in synthetic air at 300 °C was conducted providing the FeO_x/SiO₂ pre-catalyst. The pre-catalyst was reduced in 5 % H₂/N₂ at 265 °C (1 h) *in situ* prior the catalyst testing. Metal loadings by ICP-OES (wt%): 2.7 Fe.

Elemental analyses. Determination of mass fractions of carbon, hydrogen, nitrogen and sulfur were carried out on a Thermo Finnigan FlashEA 1112 Organic Elemental Analyzer. Air- or moisture sensitive samples were prepared in silver capsules inside a glove box.

Powder X-ray diffraction (XRD). XRD measurements were performed in Bragg-Brentano geometry on a D8 Advance II theta/theta diffractometer (Bruker AXS), using Ni-filtered Cu K $\alpha_{1,2}$ radiation and a position sensitive energy dispersive LynxEye silicon strip detector. The sample powder was filled into the recess of a cup-shaped sample holder, the surface of the powder bed being flush with the sample holder edge (front loading).

High-resolution transmission electron microscopy (HRTEM), scanning transmission electron microscopy (STEM) in combination with electron energy loss spectroscopy (EELS) and energy-dispersive X-ray spectroscopy (EDX). The samples were investigated on a double aberration-corrected JEOL JEM-ARM200CF transmission electron microscope. The microscope is equipped with a large-angle silicon drift EDX detector with the solid angle of 0.7 steradians from a detection area of 100 mm² and Gatan GIF Quantum 965, that allow EDX and EELS measurements, respectively. For HRTEM imaging, a Gatan OneView 4K x 4K CMOS camera was used.

Overview STEM, STEM-EDX, and particle size distributions. Overview STEM was conducted on a FEI Talos F200X microscope. The microscope was operated at an acceleration voltage of 200 kV. STEM-EDX elemental maps were recorded by a Super-X system including four silicon drift detectors. Background-corrected and fitted intensities were used for image visualization. All samples were prepared on holey carbon-coated copper grids (Plano GmbH, 400 mesh). Particle size distributions were determined by measuring of at least 250 particles with three different domains by using ImageJ software³³.

X-ray photoelectron spectroscopy (XPS). XPS was measured on K-Alpha™ + X-ray Photoelectron Spectrometer (XPS) System (Thermo Scientific), with Hemispheric 180° dual-focus analyzer with 128-channel detector. X-ray monochromator is Micro focused Al-K α radiation. For the measurement, the as-prepared samples were directly loaded onto the sample holder for measurement. The data was collected with an X-ray spot size of 200 μ m, 20 scans for survey, and 50 scans for regions.

Moessbauer Spectroscopy. Zero-field Moessbauer spectra were recorded on a SEECO MS6 spectrometer that comprises the following instruments: a JANIS CCS-850 cryostat, including a CTI-CRYOGENICS closed cycle 10 K refrigerator and a CTI-CRYOGENICS 8200 helium compressor. The cold head and sample mount are equipped with calibrated DT-670-Cu-1.4L silicon diode temperature probes and heaters. The temperature was controlled by a LAKESHORE 335 temperature controller. Spectra were recorded using an LND-45431 Kr gas proportional counter with beryllium window connected to the SEECO W204 γ -ray spectrometer that includes a high voltage supply, a 10 bit and 5 μ s ADC and two single channel analyzers. Motor control and recording of spectra was taken care of by the W304 resonant γ -ray spectrometer. For the reported spectra, a RIVERTEC MCO7.114 source (⁵⁷Co in Rh matrix) with an activity of about 1 GBq was

used. All spectra were recorded as solids in a plastic sample-holder at 13 K and data were accumulated for about 72 hours. Isomeric shifts are referenced to α -iron at room temperature.

***In situ* CO chemisorption diffuse reflectance infrared Fourier transform spectroscopy (CO-DRIFTS).** CO-DRIFTS measurements were conducted using Agilent Cary 680 and Thermo Fisher Nicolet iS50 FTIR spectrometers with MCT detectors. About 50 mg of sample was packed into a Harrick Praying Mantis low temperature reaction chamber (RhFeO_x/SiO₂ and RhFe/FeO_x/SiO₂) or a Harrick Praying Mantis high temperature reaction chamber (Rh/SiO₂) mounted in Harrick Praying Mantis diffuse reflectance attachments. RhFeO_x/SiO₂ and Rh/SiO₂ were reduced *in situ* at 260 °C in 10 % H₂/Ar for 2 h. RhFe/FeO_x/SiO₂ spent sample was mounted inside a glove box and transferred to the spectrometer under Ar atmosphere. For CO chemisorption experiments, the reaction chambers were purged with Ar (20 mL/min) at room temperature for 30 min to acquire baseline spectra. 20 mL/min of 10 % CO/Ar was then introduced for 15 min for complete CO chemisorption. The samples were again purged with pure Ar (20 mL/min), and final DRIFTS spectra were acquired at a spectral resolution of 2 cm⁻¹ and an accumulation of 128 scans.

Catalytic testing for synthesis gas conversion. The catalytic testing of the syngas-to-ethanol reaction was performed in a four-fold parallel testing unit. 0.5 g (~1 mL) of catalyst with a particle size of 100-200 μ m were loaded into each stainless-steel reactor with an effective inner diameter of 6.25 mm. The reaction temperature was monitored by temperature sensors with three thermocouples along the catalyst bed.

Four mass flow controllers were used to adjust the flow rates of the inlet gases N₂ (99.999%), CO (99.997%), H₂ (99.999%), and Ar (99.999%, all Air Liquide). The CO feed line was equipped with a carbonyl trap to remove all metal carbonyls that might be formed by high pressure of CO

in contact with stainless steel. The carbonyl trap consisted of a U-shaped ½” stainless steel tube filled with Al₂O₃ and heated to 170 °C by a heating sleeve.

Compounds in the effluent gas that condense below 180 °C were removed by a coalescence filter in the downstream oven. All remaining compounds in the effluent gas were analyzed with an online gas chromatograph (Agilent 7890B) equipped with two thermal conductivity detectors (TCD) and one flame ionization detector (FID) using He as the carrier gas. TCDs detect the inlet gases H₂, Ar, N₂, and CO as well as methane, CO₂, and H₂O. The FID is used to detect a large variety of paraffins, olefins, and oxygenates (alcohols, acetaldehyde, acetic acid) with a combination of a Porabond Q and an RTX-Wax column. The carbon balance was 96–102% for all measurements.

The catalysts were reduced *in situ* at 54 bar, 265 °C with 5 % H₂ in N₂ for 1 h with a volume flow of 58.3 mL min⁻¹. Subsequently, the temperature was decreased to 243 °C and synthesis gas feedstock mixture containing CO:H₂:N₂:Ar (20:60:10:10%, v:v) was admitted. The volume flow was kept constant to achieve a GHSV of 3500 h⁻¹. The temperature was increased to 260 °C in three steps and subsequently decreased in the same manner. Each step was held constant for at least 15 h to allow the catalysts to equilibrate.

The obtained concentrations of all compounds were corrected for volume changes due to the reaction and the subsequent N₂ dilution. Therefore, the mole fraction of Ar was used as inert internal standard according to Equation (1).

$$x_{i,corrected} = x_{i,GC} \cdot \frac{x_{Ar,bypass}}{x_{Ar,reactor}} \quad (1)$$

$x_{i,corrected}$ is the corrected mole fraction of compound i . $x_{i,reactor}$, and $x_{i,bypass}$ are the mole fractions of compound i originally obtained by the gas chromatograph sampling the respective reactor or the bypass line.

Carbon monoxide conversion X_{CO} was calculated based on the sum of carbon numbers in all products (Equation 3).

$$X_{CO} = \frac{\sum n_j C_j}{n_{CO,0}} \quad (3)$$

$n_{CO,0}$ is the mole fraction of CO in the inlet gas, and C_i is the carbon number of the product i . The selectivity S for each product i was determined based on the number of C atoms by Equation 4.

$$S_i = \frac{n_i C_i}{\sum n_{i,j} C_{i,j}} \quad (4)$$

RESULTS AND DISCUSSION

In the following, we describe the synthesis and characterization of a well-defined, freshly reduced RhFeO_x/SiO₂ model catalyst. The sample was strictly handled under a protective atmosphere to avoid any changes to its structure or chemical state during characterization. The reduced RhFeO_x/SiO₂ material was then tested for the direct conversion of synthesis gas to ethanol. The long-term stability of the RhFeO_x/SiO₂ catalyst is discussed, including the critical formation phase. A thorough characterization of the spent catalyst finally leads to clarification of a structure-function relationship, which is further proved through the synthesis of a more stable Rh/(Fe,Mn)O_x catalyst achieved by decreasing Fe mobility.

Synthesis and characterization of RhFeO_x/SiO₂ model catalyst. A single-source precursor (SSP) approach was chosen for the synthesis of a uniform RhFeO_x/SiO₂ model catalyst (Scheme 1). This approach provides a well-defined metal-metal ratio and close proximity of both metals on an atomic level by using a SSP with pre-defined metal-metal bonds.²¹ In this study, a solution of the literature-known NEt₄[RhFe₂(CO)₁₀] carbonyl cluster in tetrahydrofuran was impregnated *via* the incipient wetness method on Davisil (grade 635), a commercially available silica with a BET surface area of 480 m²/g.³⁴ The silica-supported NEt₄[RhFe₂(CO)₁₀] cluster was handled under a protective atmosphere and finally transferred into an active catalyst by thermal treatment in 10 % H₂/Ar at 260 °C. The final catalyst has a molar Rh:Fe ratio of 1:2 with nominal mass loadings of 2.8 and 3.0 wt%, respectively. Other Rh:Fe ratios can easily be attained by choosing a different SSP, e.g. [Rh₄Fe₂(CO)₁₆]²⁻ or [Rh₄Fe(CO)₁₅]⁻,³⁴ or by follow-up treatments in the form of surface-mediated synthesis.^{35,36} The as-prepared catalyst was characterized by a combination of integral characterization methods such as XRD, Moessbauer, and CO-DRIFTS as well as local methods like HRTEM, STEM combined with EDX and EELS.

Sample overview on high-angle annular dark-field (HAADF) STEM images show relatively small nanoparticles homogeneously distributed over the silica support (Fig. 1b). Particle sizes of a large set of particles from three different sample areas were measured and used to determine particle size distribution (see *Experimental Details*). The mean particle size is about 1.7 nm with a narrow distribution reflected in a small standard deviation of 0.3 nm (Fig. 1d).

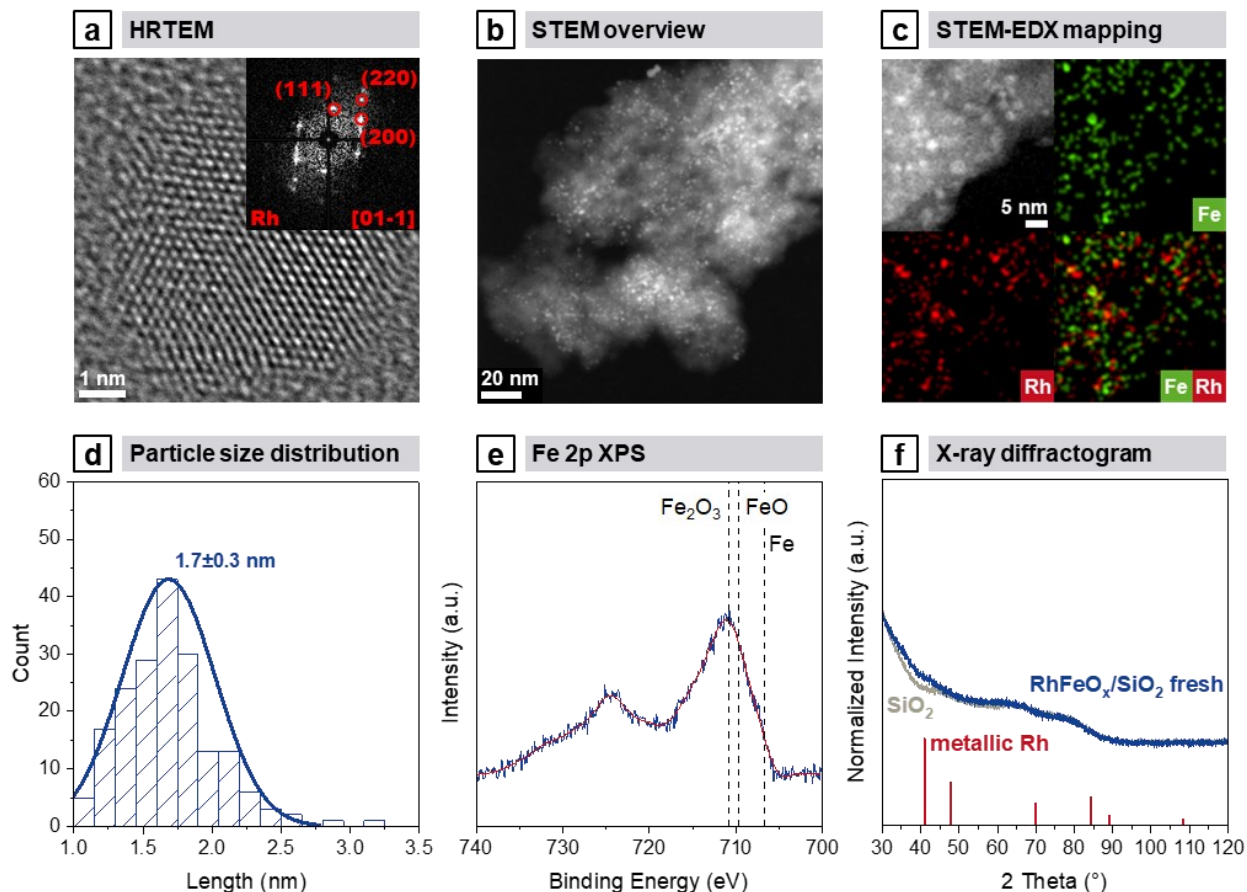


Figure 1. Structural and chemical characterization of fresh $\text{RhFeO}_x/\text{SiO}_2$ catalyst after H_2 activation at $260\text{ }^\circ\text{C}$: (a) HRTEM micrograph of relevant Rh nanoparticle viewed along $[01\text{-}1]$ zone-axis and corresponding Fast Fourier transformation (FFT) as an inset. The evaluated d -spacings are matched to fcc structure of metallic Rh; (b) HAADF-STEM overview image with corresponding (c) superposition of STEM-EDX maps of Rh L and Fe K. Individual maps of all components and respective EDX spectrum are given in the Supporting Information; (d) particle size distribution of fresh catalyst; (e) Fe 2p XPS spectra after H_2 activation; (f) X-ray diffractogram

(blue) compared to SiO₂ support (grey). Rh (red, C5-685) reference was taken from ICDD database.

XRD was performed for phase identification of the as-synthesized RhFeO_x/SiO₂ catalyst. No sharp reflections could be identified due to the XRD detection limit of supported crystallites below 3 nm (Fig. 1f).³⁷ By comparing the diffractograms of RhFeO_x/SiO₂ and Davisil, a small deviation in the region of $2\theta = 41^\circ$ is visible which might be attributable to the Rh(111) phase at $2\theta = 40.8^\circ$.

For the reason of the insufficient phase identification based on XRD investigations, lattice fringe analyses were performed on high-resolution transmission electron microscopy (HRTEM) images of size-representative crystalline particles (Fig. 1a). For these investigations, the sample was handled under an inert atmosphere and transferred to the microscope by using a vacuum transfer holder. This procedure prevents oxidation of the sample and ensures that the sample investigated is in the same oxidation state as was before catalytic testing.

The indicated lattice fringes with *d*-spacings of 2.2 and 1.9 Å are consistent with face centered cubic (fcc) {111} and {200} planes of metallic Rh (space group of Fm-3m). Metallic Fe or crystalline FeO_x particles were not observed during HRTEM imaging. This leads to the conclusion that Fe is mostly present as an amorphous oxide phase. This is also supported by XRD data where crystalline FeO_x or metallic Fe phases were not found.

The Fe oxidation state was determined by XPS without contact to an oxidative atmosphere. The RhFeO_x/SiO₂ sample shows the typical spin-orbit splitting in the Fe 2p spectrum with a peak maximum for the Fe 2p_{3/2} binding energy of 711.1 eV (Fig. 1e). This binding energy shift is typical for oxidized Fe (709.3–711.6 eV). Mossbauer spectroscopy under an inert atmosphere was conducted for an extended investigation of the Fe oxidation state. A combination of two doublets is visible, which is consistent with Fe²⁺ and Fe³⁺ doublets in reported FeO_x/SiO₂ and RhFeO_x/SiO₂ samples (Fig. S1a).³⁸

HAADF-STEM imaging combined with EDX was used to investigate the distribution of Rh and FeO_x as well as the chemical composition of the catalyst. Metallic Rh particles are in close proximity to an amorphous FeO_x phase as shown in the representative superimposed EDX mapping of Rh and Fe (Fig. 1c; for single-element maps of all components see Fig. S2). Areas in which their colors mix indicate the Rh-FeO_x interface as a result of their overlapping EDX signals. This finding is further supported by other investigated areas (Fig. S3a-d). Although the majority of particles remain small, some larger particles are found in HRTEM analysis. These particles occur as an alloyed structure after the H₂ treatment at 260 °C for 2 h (Fig. S4). It is apparent that these crystalline nanoparticles reflect a minority as no corresponding reflections could be observed in XRD (Fig. 1f). Evidence of a few larger alloyed RhFe nanoparticles suggests that the alloy formation is induced by migration of Fe on a support.

Reactivity of RhFeO_x/SiO₂ catalyst. The as-prepared RhFeO_x/SiO₂ material was tested as a catalyst for the direct conversion of StE in a fixed-bed parallel test setup at common reaction conditions for syngas chemistry (GHSV = 3500 h⁻¹, p = 54.0 bar, and T = 243–260 °C). The catalyst was compared with monometallic Rh/SiO₂ and FeO_x/SiO₂ materials at 250 and 260 °C (Table 1, entries 1–5). Modification of Rh/SiO₂ with Fe leads to increased CO conversion and enhanced selectivity towards alcohols, mainly methanol (MeOH) and ethanol (EtOH). The product distribution reported in Table 1 reveals that the increased alcohol selectivity is accompanied by the suppression of methane and C₂₊ hydrocarbon (C₂₊ HC) selectivities. Likewise, RhFeO_x/SiO₂ is less selective towards C₂₊ oxygenates, mainly acetaldehyde (AcH) and acetic acid (AcOH), as compared to the monometallic Rh/SiO₂ reference. It is consequently assumed that Fe facilitates the fast hydrogenation of acetaldehyde towards ethanol and prevents a further reaction to acetic acid. This assumption is consistent with a previously reported study about RhFe catalysts.²³

Table 1. CO Conversion and Product Selectivity from Syngas Conversion on Reference and Rh-based Catalysts^a

#	Sample	Precursor	T (°C)	H ₂ /CO	TOS (h)	r _{CO} (μmol/s/g _{Rh})	X _{CO} (%)	Product Selectivities (%)							
								CH ₄	MeOH	EtOH	AcH	AcOH	C ₂₊ _{Oxy}	C ₂₊ _{HCS}	CO ₂
1	Rh/SiO ₂	Rh ₄ (CO) ₁₂	250	3	72	22.8	2.7	49.9	2.7	6.9	8.2	14.0	4.4	11.9	2.0
2			260	3	101	27.3	3.2	52.7	3.3	7.6	6.8	12.4	4.1	11.3	1.7
3	FeO _x /SiO ₂ ^d	Fe(NO ₃) ₃	320	2	209	6.82	3.0	49.2	0.0	0.0	0.0	1.6	0.0	39.5	9.3
4	RhFeO _x /SiO ₂	[RhFe ₂ (CO) ₁₁] ^c	243	3	7	72.8	14.2	31.2	30.4	31.6	1.9	0.0	0.4	1.7	2.7
5			250	3	37	88.8	17.4	29.8	43.7	19.7	0.4	0.0	0.7	2.1	3.7
6			260	3	71	119.4	23.4	30.8	48.2	15.0	0.2	0.0	0.6	1.8	3.4
7			250	3	104	80.6	15.8	24.9	60.8	10.8	0.0	0.3	0.4	1.1	1.7
8			243	3	122	63.3	12.4	22.3	65.6	9.5	0.0	0.8	0.4	0.9	0.4
9	Rh/MnO _x	Rh(NO ₃) ₃	243	3	44	11.1	3.3	28.5	5.7	18.1	5.1	4.2	6.8	15.5	16.2
10			243	2	20	16.7	2.2	28.0	5.4	14.3	5.9	4.2	6.4	16.9	18.9
11			250	3	105	17.5	5.1	25.2	5.1	20.2	4.2	4.0	7.0	16.1	18.3
12	Rh/(Fe,Mn)O _x	[RhFe ₂ (CO) ₁₁] ^c	243	3	6	30.7	6.8	39.8	7.02	16.0	3.8	0.1	2.2	4.1	26.9
13			250	3	39	43.9	9.7	28.7	11.6	20.9	2.8	2.1	0.4	2.4	31.2
14			260	3	72	72.9	16.2	24.7	13.0	21.3	1.2	0.7	2.0	2.0	35.2
15			250	3	106	31.9	7.1	21.6	16.5	22.2	1.3	0.0	0.3	2.8	35.4
16			243	3	123	19.4	4.3	20.4	18.9	22.1	1.3	0.0	1.2	1.6	34.5

^aReaction conditions: 54.0 bar, $p(\text{H}_2) = 32.4$ bar, $p(\text{CO}) = 10.8$ bar, GHSV = 3500 h⁻¹. Product formation rates, selectivities at H₂/CO ratio of 2 and selectivities on CO₂-free basis are provided in the Support Information. ^bC₂₊ oxy includes alcohols, aldehydes, acetates, and acids. ^cC₂₊ HCs includes alkanes and alkenes. ^dMonometallic FeO_x/SiO₂ material was measured at different reaction conditions due to its low activity.

The overall oxygenate selectivity of 62.0 % is significantly higher than for other reported Fe-promoted Rh catalysts. According to a recent review, the RhFeO_x/SiO₂ catalyst is among the most selective Rh-based catalysts.¹² The molecular single-source precursor approach is thus an effective synthesis route towards more uniform model catalysts.

The FeO_x/SiO₂ reference shows negligible oxygenate selectivity. The main products are methane and higher hydrocarbons as expected for a typical Fischer-Tropsch catalyst with a Flory-Schulz distribution.³⁹ Furthermore, FeO_x/SiO₂ demonstrates water-gas shift activity resulting in a CO₂ selectivity of 9.3 %. As known from previous reports, higher Fe oxides are reduced to lower Fe oxides or metallic Fe during catalytic conversion of CO/H₂O to CO₂/H₂.⁴⁰ As a consequence, selectivity towards CO₂ can be considered as an indication for the amount of “free” FeO_x on the

catalyst support. The RhFeO_x/SiO₂ catalyst is likewise water-gas shift active with a selectivity towards CO₂ of 2.7 %. For this reason, Fe might be in an oxidized state and accessible for CO conversion. This finding is in accordance with the characterization of the as-prepared RhFeO_x/SiO₂ catalyst where it was shown that Fe is not alloyed with Rh.

Formation phase and long-term catalytic studies of RhFeO_x/SiO₂ catalyst. The RhFeO_x/SiO₂ catalyst shows only a slight deactivation from 72.8 to 63.3 μmol/s/g_{Rh} during 140 h on stream (Table 1, entries 4 and 8; for detailed TOS behavior see Fig. S5). The loss of activity is probably attributable to a change in particle size. Statistical particle size analysis of a large set of particles in different domains reveals a broader size distribution with a standard deviation of 0.6 nm (Fig. 3d). The mean particle size is significantly larger with a value of 2.4 nm. In addition to these nanoparticles, agglomerates of particles with sizes of up to 20 nm are also found (Fig. 3b).

In the case of methane, methanol, and ethanol, a significant change in selectivity could be observed (Fig. 2). The MeOH:EtOH selectivity ratio changes from 1:1 at 7 h to 7:1 at 122 h on stream. This change in selectivity is induced by a structural transformation of the RhFeO_x/SiO₂ catalysts during the catalytic conversion of syngas.

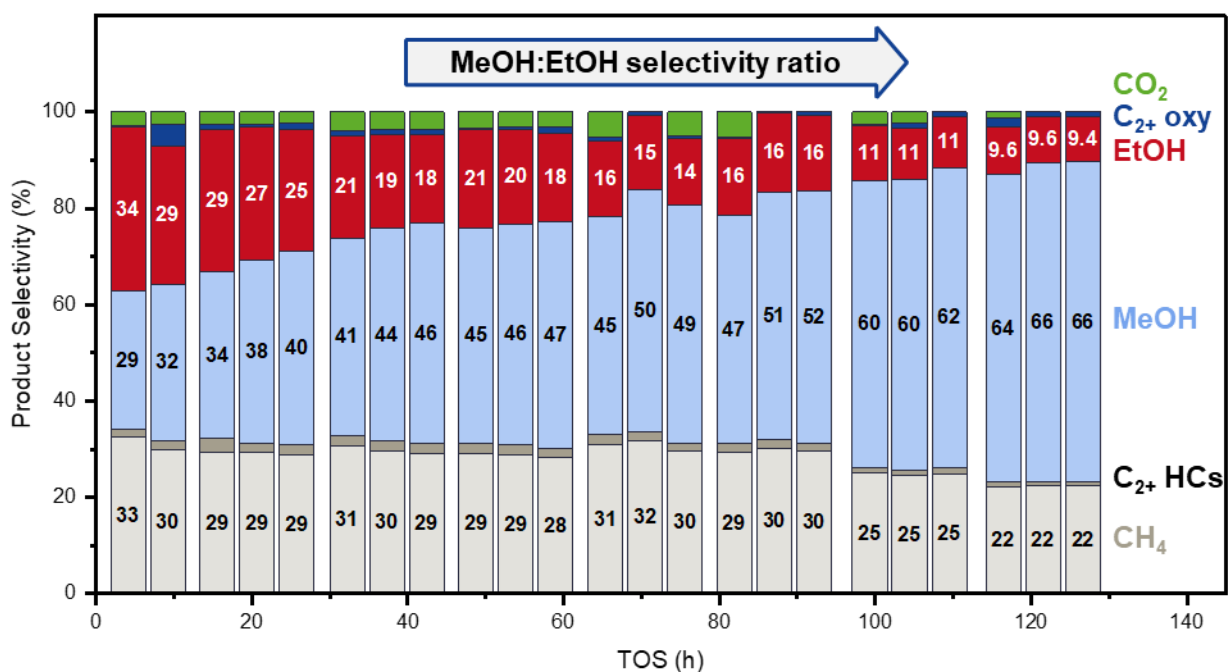


Figure 2. Product selectivities of the RhFeO_x/SiO₂ catalyst over 125 h on stream. Selectivities of methane (CH₄, light grey), C₂₊ hydrocarbons (C₂₊ HCs, dark grey), methanol (MeOH, light blue), ethanol (EtOH, red), C₂₊ oxygenates (C₂₊ oxy, dark blue), and carbon dioxide (CO₂, green) are shown. Measuring conditions: 243–260 °C, 54.0 bar, p(H₂) = 32.4 bar, p(CO) = 10.8–16.2 bar, GHSV 3500 h⁻¹. S(C₂₊ HCs) includes alkanes and alkenes. S(C₂₊ oxy) includes C₃₊ alcohols, aldehydes, acids, and acetates.

Powder XRD measurement of the spent catalyst revealed the formation of RhFe alloy crystallites with a molar composition of 1:1. The three most intense reflections are clearly visible in the corresponding diffractogram and fit to a literature-reported Rh₁Fe₁ alloy phase (ICDD C25-1408; Fig. 3f). Likewise, the detected (110) reflection at 42.70° appears exactly at the position of the reported Rh₁Fe₁ phase at 42.72°. To confirm the elemental composition of RhFe nanoparticles, STEM-EDX point analyses have been performed on several particles from different domains (Fig. S6 and Table S4). An overall Rh:Fe ratio of approx. 0.97 was determined, which is in accordance with the result obtained from XRD investigation. The crystallite size could be evaluated as 3.7 nm from the respective X-ray reflections by Scherrer equation.

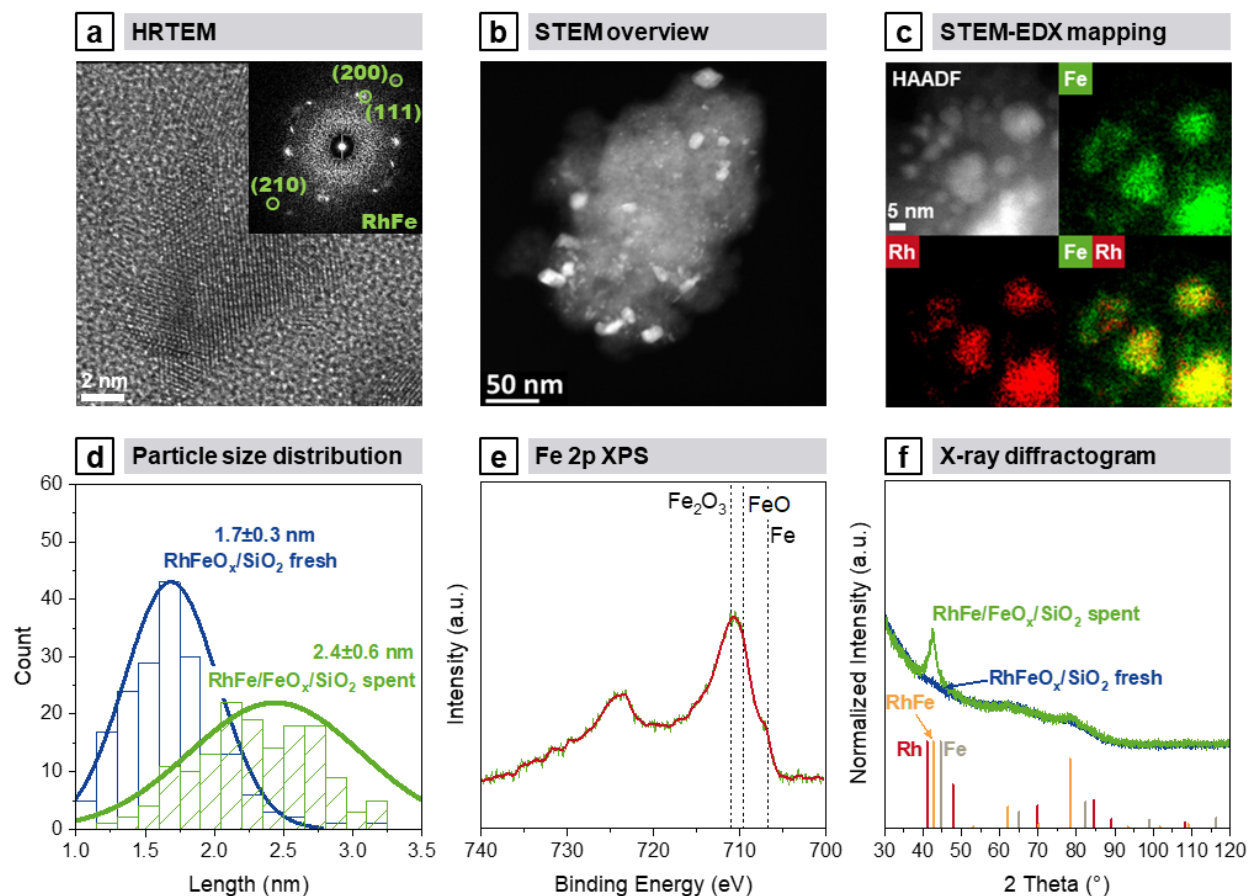


Figure 3. Structural and chemical characterization of spent RhFe/FeO_x/SiO₂ catalyst after catalytic testing: (a) HRTEM image of a representative crystalline nanoparticle and corresponding FFT as inset. The evaluated *d*-spacings are consistent with fcc planes of RhFe alloy; (b) HAADF-STEM overview image; (c) ADF-STEM image and corresponding STEM-EDX maps of Rh L, Fe K and superposition of Rh L and Fe K. Individual maps of all components and respective EDX spectrum are given in the Supporting Information; (d) particle size distribution; (e) Fe 2p XPS data; (f) X-ray diffractogram (green) in comparison with fresh RhFeO_x/SiO₂ (blue). References for Rh (red, C5-685), Fe (grey, C6-696), and Rh₁Fe₁ (orange, C25-1408) were taken from ICDD database.

Representative lattice fringe analysis on HRTEM images of smaller particles yields *d*-spacings of 2.1, 1.5, and 1.2 Å, which are consistent with {111}, {200}, and {211} lattice planes of fcc Rh₁Fe₁ alloy with the space group of Pm3m and a RhFe ratio of 1:1 (Fig. 3a). The RhFe alloy formation is also reflected in XPS and Moessbauer spectra. Fe is in a more reduced state after

catalytic testing, as indicated by a binding energy shift in the Fe 2p spectrum of -0.64 eV (Fig. 3e). This shift suggests a modification of the electronic structure, which is probably caused by the alloying of Fe and Rh. Although Fe carbide phases could lead to similar shifts in Fe 2p spectra, no indications for their formation have been found during STEM-EELS and HRTEM analyses. Furthermore, typical hyperfine splitting for a Fe carbide is absent in the respective Moessbauer spectrum (Fig. S1b). Moreover, a similar binding energy shift was observed in MnO_x-promoted RhFe/SiO₂ catalysts by Huang and co-workers.²⁰ Additionally, the partial reduction of Fe is indicated by a decrease in Fe³⁺ and Fe²⁺ doublets in Moessbauer spectroscopy (Fig. S1b). The reduced character of Fe is further confirmed by EELS. In comparison to Fe oxides, L3 and L2 edges of FeO_x are shifted to lower energies. Thus, Fe oxidation state is between 0 and 2+ (Fig. S7). Lastly, STEM-EELS spot analysis and STEM-EDX mappings visualize the RhFe alloy formation through the local enrichment of Rh and Fe in the same areas (Fig. 3c; for single-element maps of all components see Fig. S8).

As a result of the continually increasing selectivity towards methanol over time on stream, it is apparent that the RhFeO_x/SiO₂ catalyst lost C–C coupling ability, resulting in decreased ethanol formation. According to Schweicher and co-workers, the CO insertion step is crucial for chain lengthening in CO hydrogenation rather than a coupling of CH_x surface fragments.⁴¹ Thus, a loss of molecular CO adsorption sites would affect CO insertion ability and formation of higher oxygenates. CO-DRIFTS was used to identify CO adsorption modes on the RhFeO_x/SiO₂ catalyst. For this purpose, the surface sites were probed by CO adsorption at room temperature. The DRIFTS spectrum of the fresh RhFeO_x/SiO₂ catalyst shows typical vibrational bands of linear (2065 cm⁻¹) and bridged CO (1910 cm⁻¹) adsorbed on metallic Rh sites as indicated by direct comparison with a Rh/SiO₂ reference sample (Fig. S9a,b). A redshift due to RhFe surface alloy

formation, as reported for RhFe on TiO₂ and CeO₂,⁴² has not been observed. Besides these typical vibrational bands on metallic sites, two distinct bands at 2092 and 2035 cm⁻¹ were observed (Fig. S9a), which are commonly assigned to *gem*-dicarbonyl Rh⁺(CO)₂ surface species.⁴³ The typical CO band positions of CO adsorbed on metallic Rh sites and the evidence of *gem*-dicarbonyl species presupposes that Rh is unalloyed and accessible for CO adsorption in the fresh RhFeO_x/SiO₂ catalyst. Whereas the CO-DRIFTS spectrum of the spent RhFe/FeO_x/SiO₂ catalyst does not show an indication for a *gem*-dicarbonyl species and only a band at 2084 cm⁻¹ which could not be assigned to a CO adsorption mode on Rh. The disappearance of the distinct *gem*-dicarbonyl bands might be attributable to the RhFe nanoalloy formation and the decreased amount of FeO_x in close proximity to Rh. This is in accordance with Rh 3d XP spectra of the fresh RhFeO_x/SiO₂ and spent RhFe/FeO_x/SiO₂ catalysts (Fig. S10). Direct comparison of these XP spectra with a calcined and reduced Rh/SiO₂ reference sample suggests that a certain amount of oxidized Rh is present on the fresh RhFeO_x/SiO₂ sample. The oxidation state of this oxidized Rh species is probably between Rh³⁺ and Rh⁰ due to an increase intensity in the range of 308.7 and 307.7 eV. This feature disappeared on the spent RhFe/FeO_x/SiO₂ sample after catalysis, which further supposes a decrease in Rh⁺ surface sites (Fig. S10). Previous studies also demonstrated the stabilizing effect of FeO_x on *gem*-dicarbonyl Rh⁺(CO)₂ sites on RhFe/TiO₂ and RhFe/CeO₂ catalysts.^{22,44} This leads to the assumption that Rh⁺(CO)₂ surface sites are relevant for CO insertion and that their site fraction is thereby directly connected to the C–C coupling ability over CO insertion on Rh-based catalysts.

In summary, the structural transformation of unalloyed RhFeO_x to alloyed RhFe/FeO_x nanostructures during the catalytic conversion of synthesis gas leads to a continuous loss of C-C coupling ability. This nanoalloy formation is probably conditioned by high mobility of Fe on the

silica support and further affected by the reducibility of Fe at the Rh-FeO_x interface. The reduction of FeO_x occurs most likely in the vicinity of Rh through a hydrogen spillover from metallic Rh surface sites.⁴⁵ This, in turn, leads probably to a decrease in Rh-FeO_x interfacial sites, resulting in less Rh⁺ surface sites and thus less CO insertion capabilities.

From structure-function relationships to a more stable Rh/(Fe,Mn)O_x catalyst. Preventing RhFe nanoalloy formation under StE reaction conditions is vital for stable ethanol selectivities on RhFeO_x catalysts. Rh-based catalysts on silica supports suffer from high mobility of Fe, leading to increased reducibility at the Rh-FeO_x interface. Anchoring FeO_x to the support surface through strong support interactions might be one promising strategy to prevent RhFe nanoalloy formation. An extended electron microscopy study demonstrated the formation of (Fe,Mn)O_x mixed oxide phases in the multi-promoted RhMnFe/SiO₂ catalysts, which was further proved by integral characterization methods.^{19,20,46} Therefore, the formation of (Fe,Mn)O_x mixed oxides might drastically reduce the Fe mobility. For this reason, a novel high surface area Mn₂O₃ material was used as a support for the synthesis of a Rh/(Fe,Mn)O_x catalyst (Scheme 1).

The Mn₂O₃ support was synthesized through a modified, literature-known nanocasting procedure.⁴⁷ For this purpose, the ordered mesoporous silica KIT-6 was used as a template.⁴⁸ It was impregnated with a Mn acetate solution in ethanol and subsequently decomposed to a Mn₂O₃/KIT-6 composite *via* drying at 150 °C and calcination at 550 °C. The Mn₂O₃ material was characterized by BET, TEM, and ICP-OES.³⁰

Similar to the synthesis of the RhFeO_x/SiO₂ catalyst, the final Rh/(Fe,Mn)O_x catalyst was synthesized by using NEt₄[RhFe₂(CO)₁₀] as a precursor in a SSP approach. During the last step in the SSP approach, the thermal treatment in 10 % H₂/Ar at 260 °C, the porous Mn₂O₃ support was reduced to Mn₃O₄ as proved by XRD before and after thermal treatment (Fig. S11). Respective

BET analyses confirmed that the reduction was not accompanied by a change in surface area. The surface area of the freshly reduced Rh/(Fe,Mn)O_x catalyst is about 106 m²/g. Using this novel high surface area Mn₃O₄ material as a support ensures the close proximity of Rh and the metal oxide promoter. This close proximity is known to be the key requirement for enhanced performance of Rh-based catalysts in CO hydrogenation.¹⁸⁻²¹

The reduced Rh/(Fe,Mn)O_x catalyst was characterized by XRD, STEM-EDX, EDX line profile scans, and ICP-OES. Overview STEM images revealed that the particles are homogeneously distributed over the Mn₃O₄ support (Fig. 4a). Statistical particle size analysis on a large set of particles shows a mean particle size of 1.4 nm with a narrow size distribution (Fig. 4c). In comparison, the mean particle size is significantly smaller than that observed for the RhFeO_x/SiO₂ catalysts. In contrast to the RhFeO_x/SiO₂ catalyst, the FeO_x phase is well distributed over the Mn₃O₄ support and is most likely forming a mixed oxide surface structure as indicated by the STEM-EDX mapping (Fig. 4b; for single-element maps of all components see Fig. S12) and supported by XRD analysis (Fig. S11). As no indications for Fe agglomeration or particle formation are present in all investigated domains, it is assumed that Mn₃O₄ as support can drastically reduce the Fe mobility.

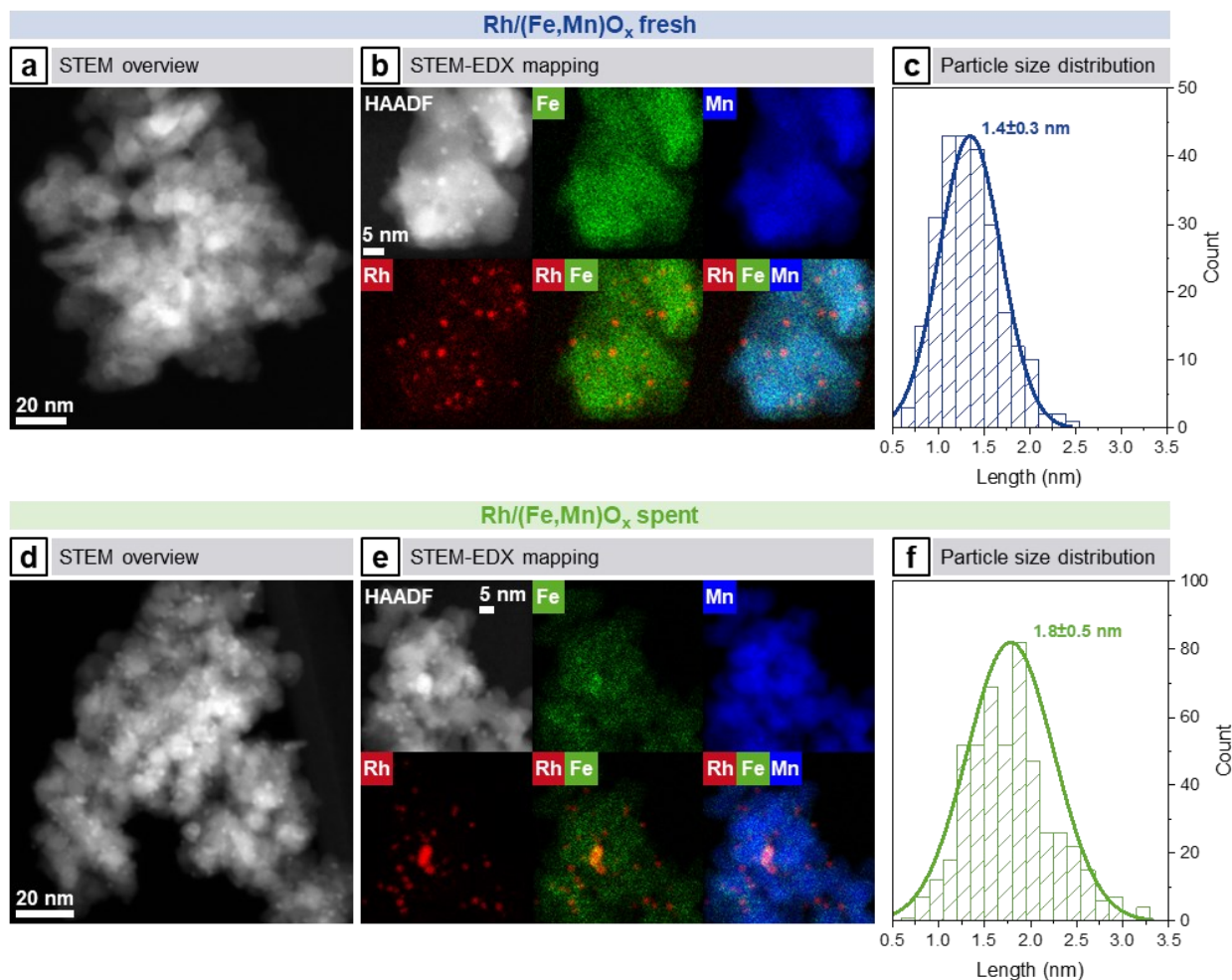


Figure 4. Morphology and chemical composition analyses of the fresh Rh/(Fe,Mn)O_x catalyst after H₂ activation: (a) HAADF-STEM overview image, (b) HAADF image and corresponding EDX mapping of Rh L, Fe K, and Mn K as well as (c) particle size distribution. For the spent Rh/(Fe,Mn)O_x catalyst after 125 h on stream: (d) HAADF-STEM overview image, (e) HAADF-STEM image and corresponding EDX mapping of Rh L, Fe K, and Mn K as well as (f) particle size distribution. Individual maps of all components and respective EDX spectra are given in the Supporting Information.

The reduced Rh/(Fe,Mn)O_x catalyst was tested for CO hydrogenation at the same reaction conditions as described above (see Reactivity of RhFeO_x/SiO₂ catalyst) and compared to a Rh/MnO_x reference material. The activity in terms of the overall CO consumption rate was more than doubled with a factor of 2.75 (Table 1, entries 9 and 12). With a slightly increased ethanol

selectivity of 22.1 % (33.7 % on CO₂-free basis; see Table S3 for CO₂-free product selectivities), the ethanol formation rate was substantially increased from 0.8 to 2.4 μmol/s/g_{Rh} at reference conditions (243 °C) and was determined with a value of 7.8 μmol/s/g_{Rh} at the best performance mark (260 °C; Table S1). Moreover, methane and C₂₊ hydrocarbons selectivities could be substantially decreased over the Rh/(Fe,Mn)O_x catalyst. However, CO₂ selectivities of up to 34.5 % have been measured, which are most likely caused by the water gas shift (WGS) reaction.^{14,23} The WGS reaction is a common side-reaction in syngas conversion.¹⁴ Thus, a competitive formation of CO₂ could be probably suppressed through an optimization of the reaction conditions, e.g., co-feeding of CO₂.^{13,49} Considering CO₂ as a side-product, the overall alcohol selectivity could be significantly increased from 30.9 to 59.8 % on a CO₂-free basis (Table S3, entries 11 and 15).

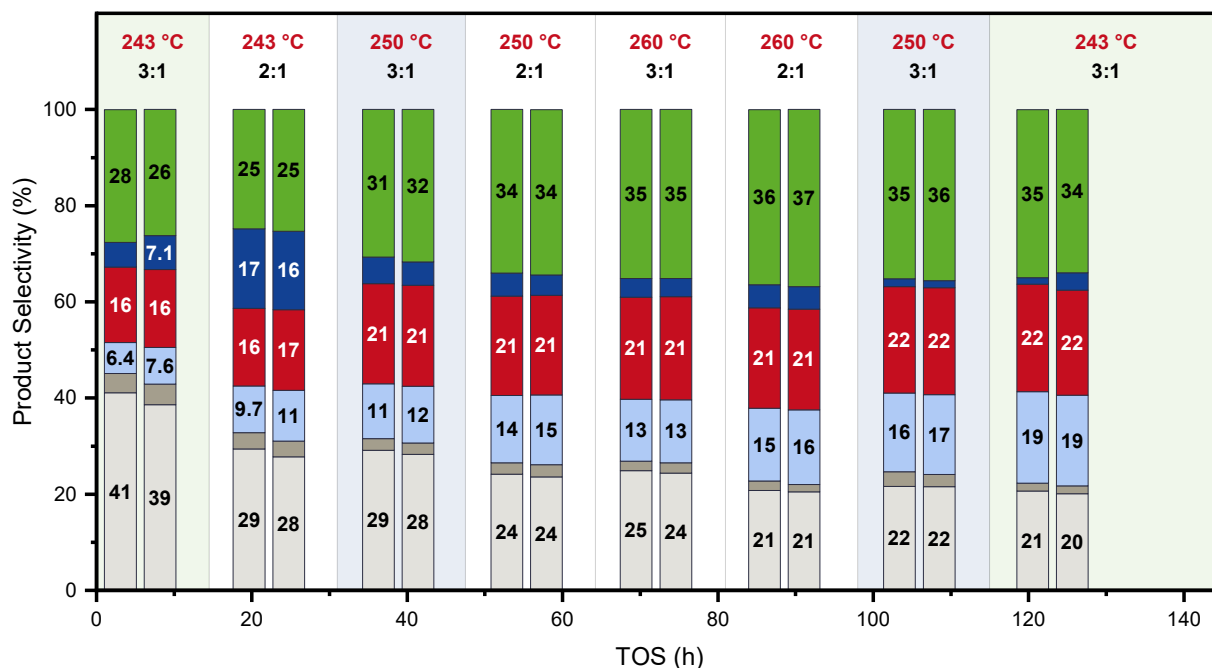


Figure 5. Product selectivities of the Rh/(Fe,Mn)O_x catalyst over 125 h on stream. Selectivities of methane (CH₄, light grey), C₂₊ hydrocarbons (C₂₊ HCs, dark grey), methanol (MeOH, light blue), ethanol (EtOH, red), C₂₊ oxygenates (C₂₊ oxy, dark blue), and carbon dioxide (CO₂, green) are shown. Measuring conditions: 243–260 °C, 54.0 bar, p(H₂) = 32.4 bar, p(CO) = 10.8 bar for

H₂:CO = 3:1 and 16.2 bar for H₂:CO = 2:1, GHSV 3500 h⁻¹. S(C₂₊ HCs) includes alkanes and alkenes. S(C₂₊ oxy) includes C₃₊ alcohols, aldehydes, acids, and acetates. For each condition two measurements are shown. Areas with same color indicate reference conditions.

In this case as well, a loss in activity was observed during the long-term catalytic test. The CO consumption rate changes from 30.7 μmol/s/g_{Rh} at 6 h to 19.4 μmol/s/g_{Rh} at 123 h on stream, which corresponds to a percentage change of -37 % (Table 1, entries 12 and 16; for detailed TOS behavior see Fig. S13). This deactivation might not be induced by particle sintering alone as the mean particle size of 1.8±0.5 nm is only slightly larger than that of the fresh Rh/(Fe,Mn)O_x catalyst with a value of 1.4±0.3 nm (Fig. 4c,f). For this reason, the active metal surface areas (SA_{metal}) of the fresh and spent Rh/(Fe,Mn)O_x catalysts have been calculated from the particle size distributions obtained by STEM. For this purpose, a cuboctahedral metal cluster model has been used (more details are provided in the Supporting Information as Fig. S14). This model demonstrates that the increase in particle diameter of the Rh/(Mn,Fe)O_x catalyst of 0.4 nm leads to a decrease in SA_{metal} from 4.04 to 3.12 m²/g_{cat}. This change in SA_{metal} of -23 % further suggests that beside particle sintering another mechanism contributes to the catalyst deactivation. Two possible pathways have been considered: blocking of active Rh sites *via* partial coverage by MnO or through coke formation.

Yang and co-workers investigated Rh/SiO₂ catalysts modified by atomic layer deposition through selective deposition of MnO as a support layer or an overlayer. A lower activity in CO hydrogenation has been observed for the MnO overlayer modified Rh/SiO₂ catalyst, and it has been subsequently assumed that the MnO overlayer may adversely block active Rh sites.¹⁸ Such a MnO overlayer has also been observed by STEM-EDX mapping of a RhMnFe/SiO₂ catalyst.²⁰ STEM-EDX area-selective analyses on the fresh and spent Rh/(Mn,Fe)O_x catalysts show that the Mn:Rh ratio has been significantly increased after catalysis (Fig. S15 and Table S4). This result

might indicate that active Rh surface sites are partially covered by MnO similar to catalysts in a reactive metal–support interaction state.⁵⁰ However, a direct atomistic confirmation, as reported for the Cu/ZnO/Al₂O₃ methanol synthesis catalyst, is required for a clear proof.⁵¹

Another possible explanation for the deactivation might be coke formation as proofed by elemental analysis before and after catalysis. The carbon content increased from 0.16 on the fresh to 1.53 wt% on the spent Rh/(Fe,Mn)O_x sample. As MnCO₃ has been formed during catalysis and contributes to the increase in carbon content, phase composition analysis has been performed through Rietveld refinement of the corresponding X-ray diffractogram (Fig. S16). The relative amount of carbon, which could not be attributed to MnCO₃ formation, is about 0.49 wt%. This amount seems to be relatively low compared to coke formation on reforming and dehydrogenation catalyst, which usually ranges from 6–9 wt%.^{52–54} Notwithstanding, the increased amount of carbon on the Rh/(Fe,Mn)O_x suggests that coke formation might also contribute to its deactivation.

After a relatively short formation phase of 35 h on stream, the ethanol selectivity was stable and did not change during the remaining 90 h on stream (Fig. 5). We reason that this stability in ethanol selectivity is a consequence of stable, metallic Rh nanostructures which are not alloyed with Fe. This assumption is in accordance with a recent *in situ* XRD study of MnRh/Fe₂O₃ catalysts, correlating increased ethanol selectivities with MnO, FeO_x, and mixed (Fe,Mn)O_x phases in vicinity to Rh.⁴⁴ As previously mentioned, Fe might be less mobile on the MnO_x support due to the strong support interaction resulting from the formation of a mixed (Fe,Mn)O_x surface oxide. This might decrease the Fe mobility as well as preventing further reduction of FeO_x at the Rh-FeO_x interface. We also proved the formation of such a mixed (Fe,Mn)O_x surface oxide in the spent catalysts after the formation phase and long-term catalytic studies. STEM-EDX mapping and line scanning profile analyses were performed (Fig. 6b,c; for corresponding STEM image and

single-elements maps see Fig. 4e) for this purpose. While the EDX map already indicates a homogenous distribution of Fe over the MnO_x support (Fig. 4e), the representative elemental line profile analysis provides further confirmation for the well-defined $(\text{Fe,Mn})\text{O}_x$ surface oxide structure (Fig. 6b). Similar to the fresh $\text{Rh}/(\text{Fe,Mn})\text{O}_x$ catalyst (Fig. 4a–c), Fe agglomeration or particle formation were not observed (Fig. 4d,e). Consequently, not even high pressures of synthesis gas could cause increased Fe mobility. The formation of a $(\text{Fe,Mn})\text{O}_x$ mixed oxide further affected the expected MnO reflections in the corresponding X-ray diffractogram of the spent $\text{Rh}/(\text{Fe,Mn})\text{O}_x$ sample (Fig. 6a). The observed MnO reflections are slightly shifted to higher angles as expected for $(\text{Mn,Fe})\text{O}_x$ mixed oxide phases indicating the incorporation of FeO at the surface. Reflections from RhFe crystallites have not been observed, which is in accordance with STEM-EDX results.

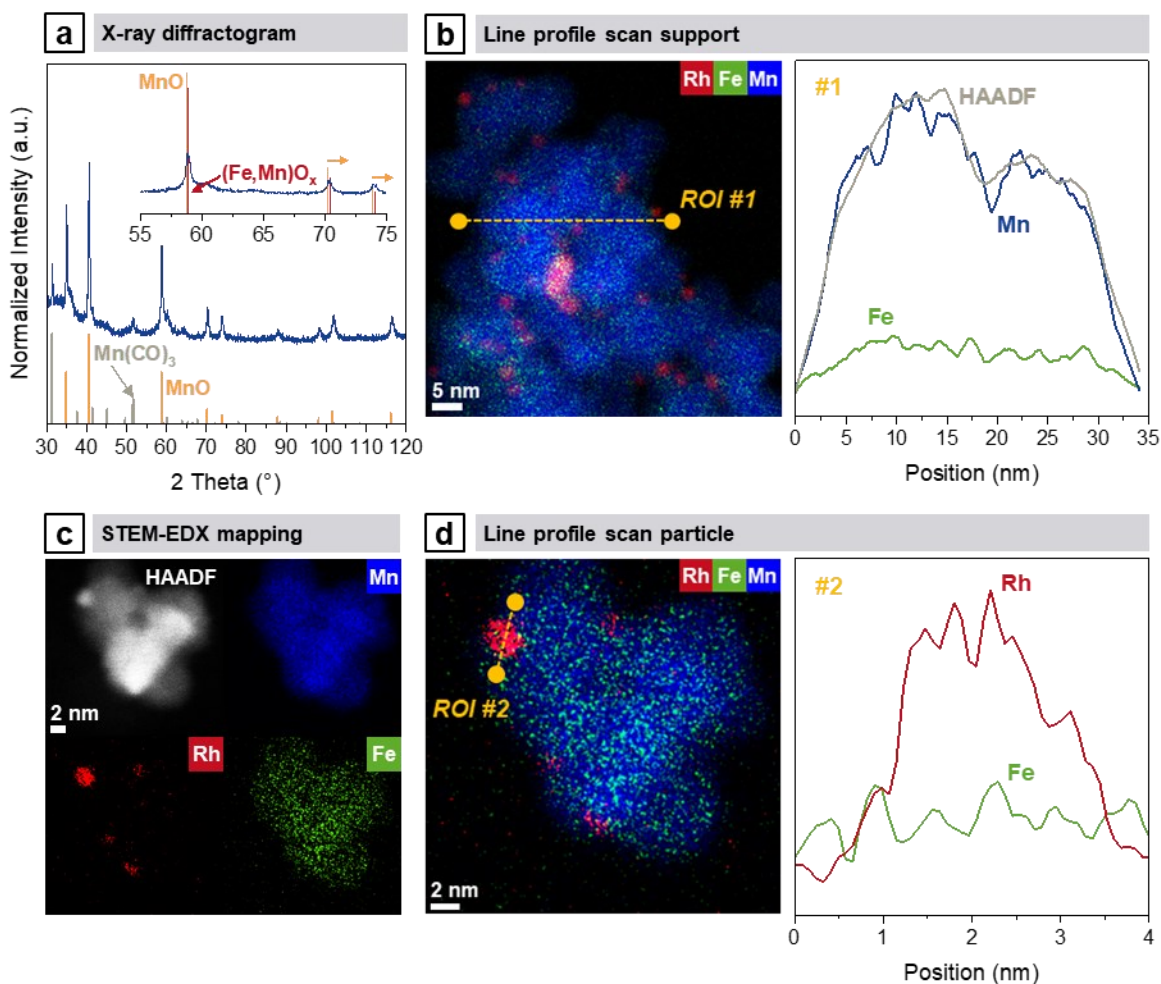


Figure 6. Phase identification and extended electron microscopy analysis of spent Rh/(Fe,Mn)O_x catalyst: **(a)** X-ray diffractogram (blue) with a detailed view of the mixed oxide induced reflection shifts as inset. References for MnO (orange, C7-230), MnCO₃ (grey, C44-1472), and (Fe,Mn)O_x (red, C77-2362) were taken from ICDD database. Chemical formula of (Fe,Mn)O_x mixed oxide reference is (FeO)_{0.099}(MnO)_{0.901}. Additional diffractogram with reference patterns of RhFe and Rh is provided in the Supporting Information; **(b)** superposition of STEM-EDX maps of Rh L, Fe K, and Mn K with line scan path highlighted in yellow (ROI #1) and corresponding line scan profiles of Fe K (green), Mn K (blue) and HAADF (grey) intensities; **(c)** high-resolution STEM image and corresponding EDX mapping of Rh L, Fe K, and Mn K; **(d)** superposition of STEM-EDX maps of Rh L, Fe K, and Mn K with line scan path over a representative Rh particle (red) highlighted in yellow (ROI #2) and corresponding line scan profiles of Rh L (red) and Fe K (green). Individual maps of all components and respective EDX spectrum are given in the Supporting Information.

Additional STEM-EDX elemental line scans at high magnifications confirmed the unalloyed state of the observed Rh nanoparticles in the spent Rh/(Fe,Mn)O_x catalyst (Fig. 6d; corresponding STEM image and single-element maps see Fig. S17). The representative line profiles of Rh and Fe clearly demonstrate that there is no local enrichment of Fe in areas of increased Rh intensity (Fig. 6d). These local enrichments are essential to form RhFe alloyed nanostructures as present in RhFe/FeO_x/SiO₂ after catalysis (for line-profile scans see Fig. S18).

In brief, the use of high surface area MnO_x as support for RhFe catalysts decreases Fe mobility through the formation of mixed (Fe,Mn)O_x surface oxides. As a reason of the decreased Fe mobility and reducibility, the formation of RhFe nanoalloyed structures is unfavored on MnO_x as support and thereby Rh remains in a stable metallic state.

CONCLUSION

The formation phase of a RhFeO_x/SiO₂ catalyst was identified to be critical in CO hydrogenation to ethanol. Herein, we reported a generic method for investigating this critical phase at high partial pressure of synthesis gas. During a long-term catalytic test, a significant change in oxygenate selectivity was observed. Combining integral and local characterization methods (XPS, XRD, HRTEM, HAADF, STEM-EELS, and STEM-EDX), we could ascribe this dynamic behavior to a structural transformation of an unalloyed RhFeO_x to an alloyed RhFe/FeO_x nanostructure. This transformation was probably induced by high mobility of Fe and led to the continuous loss of C–C coupling and thus also to a decrease in ethanol formation abilities. Finally, these selectivity dependencies on the nanostructure of RhFe catalysts provide an explanation for the great variations in reported results of catalytic reactivity and different proposed structure models of the active phase, which range from unalloyed over core-shell to alloyed RhFe nanostructures.

The structure-function relationship we identified finally provides the opportunity for new catalyst design strategies: decreasing Fe mobility and reducibility is vital to improve Fe-promoted Rh catalysts and should lead to more stable catalysts in terms of ethanol selectivity. As one example, we reported the usage of a novel high surface area Mn₂O₃ material as a support. It was shown that the formation of a (Fe,Mn)O_x mixed surface oxide drastically reduces the Fe mobility. Anchoring FeO_x on the Mn₂O₃ surface through strong support interactions prevents the formation of RhFe nanoalloy structures and led to stable ethanol selectivities during a long-term catalytic study.

In summary, the reported generic method of investigating the critical formation phase provides meaningful insights into the structural behavior of catalysts under reaction conditions and addresses explanations for controversially discussed catalytic results. We foresee that this method

will not remain limited to Rh-based catalysts in CO hydrogenation and will be applicable to many other catalyst systems, such as CuCo/SiO₂ or PtCo/SiO₂, and other hydrogenation reactions.

AUTHOR INFORMATION

Corresponding Author

*Email: r.naumann@bascat.tu-berlin.de

ASSOCIATED CONTENT

Supporting Information. The Supporting Information is available free of charge on the ACS Publications website. Moessbauer spectra, additional STEM-EDX maps and spectra, HRTEM, STEM-EDX point analysis and line profile scans, CO-DRIFTS, and EELS of RhFeO_x/SiO₂; XRD, additional STEM-EDX maps and spectra, STEM-EDX area-selective analyses, Rietveld refinement, details of cuboctahedral model of Rh/(Fe,Mn)O_x; CO consumption rates over TOS, product formation rates, selectivities on CO₂-free basis of RhFeO_x/SiO₂ and Rh/(Fe,Mn)O_x.

ACKNOWLEDGMENT

This work was conducted in the framework of the BasCat collaboration between BASF SE, TU Berlin, Fritz Haber Institute (FHI) of the Max Planck Society and was partially funded by the Deutsche Forschungsgemeinschaft (DFG, German Research Foundation) under Germany's Excellence Strategy – EXC 2008 – 390540038 – UniSysCat. We would like to thank Dr. Frank Girgsdies for XRD, Dr. Shuang Li for XPS, Jutta Kröhnert and Dr. Annette Trunschke for DRIFTS, Dr. Matthias Keck and Prof. Dr. Christian Limberg for Moessbauer measurements, Dr. Miriam Klapproth for assistance during synthesis of the MnO_x support, Katharina Trapp and Danielle Czarnowske for their assistance in laboratory work and Stephen Lohr for technical assistance. We would like to gratefully acknowledge Dr. Walid Hetaba and Dr. Thomas Lunkenbein for the opportunity to be part of the ChemiTEM project at the FHI.

REFERENCES

- (1) Chen, S.; Abdel-Mageed, A. M.; Li, D.; Bansmann, J.; Cisneros, S.; Biskupek, J.; Huang, W.; Behm, R. J. Morphology-Engineered Highly Active and Stable Ru/TiO₂ Catalysts for Selective CO Methanation. *Angew. Chem. Int. Ed.* **2019**, *58* (31), 10732–10736. <https://doi.org/10.1002/anie.201903882>.
- (2) Rezvani, A.; Abdel-Mageed, A. M.; Ishida, T.; Murayama, T.; Parlinska-Wojtan, M.; Behm, R. J. CO₂ Reduction to Methanol on Au/CeO₂ Catalysts: Mechanistic Insights from Activation/Deactivation and SSITKA Measurements. *ACS Catal.* **2020**, *10* (6), 3580–3594. <https://doi.org/10.1021/acscatal.9b04655>.
- (3) Abdel-Mageed, A. M.; Klyushin, A.; Knop-Gericke, A.; Schlögl, R.; Behm, R. J. Influence of CO on the Activation, O-Vacancy Formation, and Performance of Au/ZnO Catalysts in CO₂ Hydrogenation to Methanol. *J. Phys. Chem. Lett.* **2019**, *10* (13), 3645–3653. <https://doi.org/10.1021/acs.jpcclett.9b00925>.
- (4) Bergmann, A.; Roldan Cuenya, B. Operando Insights into Nanoparticle Transformations during Catalysis. *ACS Catal.* **2019**, *9* (11), 10020–10043. <https://doi.org/10.1021/acscatal.9b01831>.
- (5) Yang, N.; Medford, A. J.; Liu, X.; Studt, F.; Bligaard, T.; Bent, S. F.; Nørskov, J. K. Intrinsic Selectivity and Structure Sensitivity of Rhodium Catalysts for C₂+ Oxygenate Production. *J. Am. Chem. Soc.* **2016**, *138* (11), 3705–3714. <https://doi.org/10.1021/jacs.5b12087>.
- (6) Hartman, T.; Geitenbeek, R. G.; Whiting, G. T.; Weckhuysen, B. M. Operando Monitoring of Temperature and Active Species at the Single Catalyst Particle Level. *Nat.*

- Catal.* **2019**, 2 (11), 986–996. <https://doi.org/10.1038/s41929-019-0352-1>.
- (7) Fischer, N.; Claeys, M. In Situ Characterization of Fischer–Tropsch Catalysts: A Review. *J. Phys. D: Appl. Phys.* **2020**, 53 (29), 293001. <https://doi.org/10.1088/1361-6463/ab761c>.
- (8) Tinnemans, S. J.; Kox, M. H. F.; Sletering, M. W.; Nijhuis, T. A. (Xander); Visser, T.; Weckhuysen, B. M. Dealing with a Local Heating Effect When Measuring Catalytic Solids in a Reactor with Raman Spectroscopy. *Phys. Chem. Chem. Phys.* **2006**, 8 (20), 2413. <https://doi.org/10.1039/b602311h>.
- (9) Meunier, F. C. The Design and Testing of Kinetically-Appropriate Operando Spectroscopic Cells for Investigating Heterogeneous Catalytic Reactions. *Chem. Soc. Rev.* **2010**, 39 (12), 4602. <https://doi.org/10.1039/b919705m>.
- (10) Bañares, M. A.; Guerrero-Pérez, M. O.; Fierro, J. L. G.; Cortez, G. G. Raman Spectroscopy during Catalytic Operations with On-Line Activity Measurement (Operando Spectroscopy): A Method for Understanding the Active Centres of Cations Supported on Porous Materials. *J. Mater. Chem.* **2002**, 12 (11), 3337–3342. <https://doi.org/10.1039/B204494C>.
- (11) Goodman, E. D.; Johnston-Peck, A. C.; Dietze, E. M.; Wrasman, C. J.; Hoffman, A. S.; Abild-Pedersen, F.; Bare, S. R.; Plessow, P. N.; Cargnello, M. Catalyst Deactivation via Decomposition into Single Atoms and the Role of Metal Loading. *Nat. Catal.* **2019**, 2 (9), 748–755. <https://doi.org/10.1038/s41929-019-0328-1>.
- (12) Luk, H. T.; Mondelli, C.; Ferré, D. C.; Stewart, J. A.; Pérez-Ramírez, J. Status and Prospects in Higher Alcohols Synthesis from Syngas. *Chem. Soc. Rev.* **2017**, 46 (5),

- 1358–1426. <https://doi.org/10.1039/C6CS00324A>.
- (13) Subramani, V.; Gangwal, S. K. A Review of Recent Literature to Search for an Efficient Catalytic Process for the Conversion of Syngas to Ethanol. *Energy & Fuels* **2008**, *22* (2), 814–839. <https://doi.org/10.1021/ef700411x>.
- (14) Spivey, J. J.; Egbebi, A. Heterogeneous Catalytic Synthesis of Ethanol from Biomass-Derived Syngas. *Chem. Soc. Rev.* **2007**, *36* (9), 1514. <https://doi.org/10.1039/b414039g>.
- (15) Gu, T.; Wang, B.; Chen, S.; Yang, B. Automated Generation and Analysis of the Complex Catalytic Reaction Network of Ethanol Synthesis from Syngas on Rh(111). *ACS Catal.* **2020**, *10* (11), 6346–6355. <https://doi.org/10.1021/acscatal.0c00630>.
- (16) Ao, M.; Pham, G. H.; Sunarso, J.; Tade, M. O.; Liu, S. Active Centers of Catalysts for Higher Alcohol Synthesis from Syngas: A Review. *ACS Catal.* **2018**, *8* (8), 7025–7050. <https://doi.org/10.1021/acscatal.8b01391>.
- (17) Schumann, J.; Medford, A. J.; Yoo, J. S.; Zhao, Z.-J.; Bothra, P.; Cao, A.; Studt, F.; Abild-Pedersen, F.; Nørskov, J. K. Selectivity of Synthesis Gas Conversion to C₂+ Oxygenates on fcc(111) Transition-Metal Surfaces. *ACS Catal.* **2018**, *8* (4), 3447–3453. <https://doi.org/10.1021/acscatal.8b00201>.
- (18) Yang, N.; Yoo, J. S.; Schumann, J.; Bothra, P.; Singh, J. A.; Valle, E.; Abild-Pedersen, F.; Nørskov, J. K.; Bent, S. F. Rh-MnO Interface Sites Formed by Atomic Layer Deposition Promote Syngas Conversion to Higher Oxygenates. *ACS Catal.* **2017**, *7* (9), 5746–5757. <https://doi.org/10.1021/acscatal.7b01851>.
- (19) Dimitrakopoulou, M.; Huang, X.; Kröhnert, J.; Teschner, D.; Praetz, S.; Schlesiger, C.;

- Malzer, W.; Janke, C.; Schwab, E.; Rosowski, F.; Kaiser, H.; Schunk, S.; Schlögl, R.; Trunschke, A. Insights into Structure and Dynamics of (Mn,Fe)O_x-Promoted Rh Nanoparticles. *Faraday Discuss.* **2018**, *208*, 207–225.
<https://doi.org/10.1039/C7FD00215G>.
- (20) Huang, X.; Teschner, D.; Dimitrakopoulou, M.; Fedorov, A.; Frank, B.; Kraehnert, R.; Rosowski, F.; Kaiser, H.; Schunk, S.; Kuretschka, C.; Schlögl, R.; Willinger, M.-G.; Trunschke, A. Atomic-Scale Observation of the Metal–Promoter Interaction in Rh-Based Syngas-Upgrading Catalysts. *Angew. Chem. Int. Ed.* **2019**, *58* (26), 8709–8713.
<https://doi.org/10.1002/anie.201902750>.
- (21) Preikschas, P.; Bauer, J.; Huang, X.; Yao, S.; Naumann d’Alnoncourt, R.; Kraehnert, R.; Trunschke, A.; Rosowski, F.; Driess, M. From a Molecular Single-Source Precursor to a Selective High-Performance RhMnO_x Catalyst for the Conversion of Syngas to Ethanol. *ChemCatChem* **2019**, *11* (2), 885–892. <https://doi.org/10.1002/cctc.201801978>.
- (22) Haider, M.; Gogate, M.; Davis, R. Fe-Promotion of Supported Rh Catalysts for Direct Conversion of Syngas to Ethanol. *J. Catal.* **2009**, *261* (1), 9–16.
<https://doi.org/10.1016/j.jcat.2008.10.013>.
- (23) Liu, Y.; Göeltl, F.; Ro, I.; Ball, M. R.; Sener, C.; Aragão, I. B.; Zanchet, D.; Huber, G. W.; Mavrikakis, M.; Dumesic, J. A. Synthesis Gas Conversion over Rh-Based Catalysts Promoted by Fe and Mn. *ACS Catal.* **2017**, *7* (7), 4550–4563.
<https://doi.org/10.1021/acscatal.7b01381>.
- (24) Wang, J.; Zhang, Q.; Wang, Y. Rh-Catalyzed Syngas Conversion to Ethanol: Studies on the Promoting Effect of FeO_x. *Catal. Today* **2011**, *171* (1), 257–265.

<https://doi.org/10.1016/j.cattod.2011.03.023>.

- (25) Burch, R.; Petch, M. I. Investigation of the Reactions of Acetaldehyde on Promoted Rhodium Catalysts. *Appl. Catal. A* **1992**, *88* (1), 61–76. [https://doi.org/10.1016/0926-860X\(92\)80196-J](https://doi.org/10.1016/0926-860X(92)80196-J).
- (26) Burch, R.; Hayes, M. J. The Preparation and Characterisation of Fe-Promoted Al₂O₃-Supported Rh Catalysts for the Selective Production of Ethanol from Syngas. *J. Catal.* **1997**, *165* (2), 249–261. <https://doi.org/10.1006/jcat.1997.1482>.
- (27) Gogate, M. R.; Davis, R. J. X-Ray Absorption Spectroscopy of an Fe-Promoted Rh/TiO₂ Catalyst for Synthesis of Ethanol from Synthesis Gas. *ChemCatChem* **2009**, *1* (2), 295–303. <https://doi.org/10.1002/cctc.200900104>.
- (28) Mo, X.; Gao, J.; Umnajkaseam, N.; Goodwin Jr., J. G. La, V, and Fe Promotion of Rh/SiO₂ for CO Hydrogenation: Effect on Adsorption and Reaction. *J. Catal.* **2009**, *267* (2), 167–176. <https://doi.org/10.1016/j.jcat.2009.08.007>.
- (29) Carrillo, P.; Shi, R.; Teeluck, K.; Senanayake, S. D.; White, M. G. In Situ Formation of FeRh Nanoalloys for Oxygenate Synthesis. *ACS Catal.* **2018**, *8* (8), 7279–7286. <https://doi.org/10.1021/acscatal.8b02235>.
- (30) Palomino, R. M.; Magee, J. W.; Llorca, J.; Senanayake, S. D.; White, M. G. The Effect of Fe-Rh Alloying on CO Hydrogenation to C₂₊ Oxygenates. *J. Catal.* **2015**, *329*, 87–94. <https://doi.org/10.1016/j.jcat.2015.04.033>.
- (31) Klapproth, M. Synthesis of High Surface Area Metal Oxides and Supported Metal Oxide Catalysts for the Oxidative Coupling of Methane. Doctoral Thesis, Technische Universität

Berlin, December 2017. <https://doi.org/10.14279/depositonce-6881>.

- (32) Guzman-Jimenez, I. Y.; van Hal, J. W.; Whitmire, K. H. Metal Cluster Catalysis: A Kinetic and Mechanistic Study of the Carbonylation of Methanol to Give Methyl Formate as Catalyzed by $[\text{Et}_4\text{N}]_2[\text{Fe}_3(\text{CO})_9\text{E}]$ (E = S, Se, Te). *Organometallics* **2003**, *22* (9), 1914–1922. <https://doi.org/10.1021/om020548+>.
- (33) Schneider, C. A.; Rasband, W. S.; Eliceiri, K. W. NIH Image to ImageJ: 25 Years of Image Analysis. *Nat. Methods* **2012**, *9* (7), 671–675. <https://doi.org/10.1038/nmeth.2089>.
- (34) Ceriotti, A.; Longoni, G.; Pergola, R. Della; Heaton, B. T.; Smith, D. O. Bimetallic Iron–Rhodium Anionic Carbonyl Clusters: $[\text{Fe}_2\text{Rh}(\text{CO})_x]^-$ (X= 10 or 11), $[\text{FeRh}_4(\text{CO})_{15}]^{2-}$, $[\text{Fe}_2\text{Rh}_4(\text{CO})_{16}]^{2-}$, and $[\text{FeRh}_5(\text{CO})_{16}]^-$. *J. Chem. Soc., Dalt. Trans.* **1983**, *3* (7), 1433–1440. <https://doi.org/10.1039/DT9830001433>.
- (35) Xu, Z.; Kawi, S.; Rheingold, A. L.; Gates, B. C. Surface-Mediated Synthesis of $[\text{PtRh}_5(\text{CO})_{15}]^-$ on MgO. *Inorg. Chem.* **1994**, *33* (19), 4415–4417. <https://doi.org/10.1021/ic00097a036>.
- (36) Cariati, E.; Dragonetti, C.; Roberto, D.; Ugo, R.; Lucenti, E. Surface-Mediated Organometallic Synthesis: High-Yield Syntheses of $[\text{Rh}_4(\text{CO})_{12}]$, $[\text{Rh}_6(\text{CO})_{16}]$, $[\text{Rh}_5(\text{CO})_{15}]^-$ and $[\text{Rh}_{12}(\text{CO})_{30}]^{2-}$ by Controlled Reduction of Silica-Supported RhCl_3 or $[\text{Rh}(\text{CO})_2\text{Cl}]_2$ in the Presence of $\text{CH}_3\text{CO}_2\text{Na}$, Na_2CO_3 or K_2CO_3 . *Inorganica Chim. Acta* **2003**, *349*, 189–194. [https://doi.org/10.1016/S0020-1693\(03\)00029-X](https://doi.org/10.1016/S0020-1693(03)00029-X).
- (37) O’Connell, K.; Regalbuto, J. R. High Sensitivity Silicon Slit Detectors for 1 nm Powder XRD Size Detection Limit. *Catal. Letters* **2015**, *145* (3), 777–783.

<https://doi.org/10.1007/s10562-015-1479-6>.

- (38) Niemantsverdriet, J. W.; Van der Kraan, A. M.; Van Loef, J. J.; Delgass, W. N. In Situ Moessbauer Spectroscopy of Bimetallic Iron-Rhodium (FeRh)/Silica Catalysts at 295 K. *J. Phys. Chem.* **1983**, *87* (8), 1292–1294. <https://doi.org/10.1021/j100231a005>.
- (39) Zhang, C.-H.; Wan, H.-J.; Yang, Y.; Xiang, H.-W.; Li, Y.-W. Study on the Iron–Silica Interaction of a Co-Precipitated Fe/SiO₂ Fischer–Tropsch Synthesis Catalyst. *Catal. Commun.* **2006**, *7* (9), 733–738. <https://doi.org/10.1016/j.catcom.2006.03.018>.
- (40) Zhu, M.; Wachs, I. E. Iron-Based Catalysts for the High-Temperature Water–Gas Shift (HT-WGS) Reaction: A Review. *ACS Catal.* **2016**, *6* (2), 722–732. <https://doi.org/10.1021/acscatal.5b02594>.
- (41) Schweicher, J.; Bundhoo, A.; Kruse, N. Hydrocarbon Chain Lengthening in Catalytic CO Hydrogenation: Evidence for a CO-Insertion Mechanism. *J. Am. Chem. Soc.* **2012**, *134* (39), 16135–16138. <https://doi.org/10.1021/ja3068484>.
- (42) Magee, J. W.; Palomino, R. M.; White, M. G. Infrared Spectroscopy Investigation of Fe-Promoted Rh Catalysts Supported on Titania and Ceria for CO Hydrogenation. *Catal. Lett.* **2016**, *146* (9), 1771–1779. <https://doi.org/10.1007/s10562-016-1801-y>.
- (43) Yang, C.; Garl, C. W. Infrared Studies of Carbon Monoxide Chemisorbed on Rhodium. *J. Phys. Chem.* **1957**, *61* (11), 1504–1512. <https://doi.org/10.1021/j150557a013>.
- (44) Liu, W.; Wang, S.; Sun, T.; Wang, S. The Promoting Effect of Fe Doping on Rh/CeO₂ for the Ethanol Synthesis. *Catal. Letters* **2015**, *145* (9), 1741–1749. <https://doi.org/10.1007/s10562-015-1577-5>.

- (45) Lebedeva, O. E.; Chiou, W.-A.; Sachtler, W. M. H. Metal Migration from Zeolites onto Iron Oxide: An Alternative to Hydrogen Spillover. *J. Catal.* **1999**, *188* (2), 365–374. <https://doi.org/10.1006/jcat.1999.2680>.
- (46) Carrillo, P.; Shi, R.; Senanayake, S. D.; White, M. G. In Situ Structural Study of Manganese and Iron Oxide Promoted Rhodium Catalysts for Oxygenate Synthesis. *Appl. Catal. A*. **2020**, *608*, 117845. <https://doi.org/10.1016/j.apcata.2020.117845>.
- (47) Smått, J.-H.; Weidenthaler, C.; Rosenholm, J. B.; Lindén, M. Hierarchically Porous Metal Oxide Monoliths Prepared by the Nanocasting Route. *Chem. Mater.* **2006**, *18* (6), 1443–1450. <https://doi.org/10.1021/cm051880p>.
- (48) Choi, M.; Heo, W.; Kleitz, F.; Ryoo, R. Facile Synthesis of High Quality Mesoporous SBA-15 with Enhanced Control of the Porous Network Connectivity and Wall Thickness. *Chem. Commun.* **2003**, *3* (12), 1340–1341. <https://doi.org/10.1039/B303696K>.
- (49) Zhou, W.; Zhou, C.; Yin, H.; Shi, J.; Zhang, G.; Zheng, X.; Min, X.; Zhang, Z.; Cheng, K.; Kang, J.; Zhang, Q.; Wang, Y. Direct Conversion of Syngas into Aromatics over a Bifunctional Catalyst: Inhibiting Net CO₂ Release. *Chem. Commun.* **2020**, *56* (39), 5239–5242. <https://doi.org/10.1039/D0CC00608D>.
- (50) Penner, S.; Armbrüster, M. Formation of Intermetallic Compounds by Reactive Metal-Support Interaction: A Frequently Encountered Phenomenon in Catalysis. *ChemCatChem* **2015**, *7* (3), 374–392. <https://doi.org/10.1002/cctc.201402635>.
- (51) Behrens, M.; Studt, F.; Kasatkin, I.; Kuhl, S.; Havecker, M.; Abild-Pedersen, F.; Zander, S.; Girgsdies, F.; Kurr, P.; Knief, B.-L.; Tovar, M.; Fischer, R. W.; Nørskov, J. K.;

- Schlögl, R. The Active Site of Methanol Synthesis over Cu/ZnO/Al₂O₃ Industrial Catalysts. *Science* **2012**, 336 (6083), 893–897. <https://doi.org/10.1126/science.1219831>.
- (52) Martín, N.; Viniegra, M.; Zarate, R.; Espinosa, G.; Batina, N. Coke Characterization for an Industrial Pt–Sn/ γ -Al₂O₃ Reforming Catalyst. *Catal. Today* **2005**, 107–108, 719–725. <https://doi.org/10.1016/j.cattod.2005.07.002>.
- (53) Ingale, P.; Guan, C.; Kraehnert, R.; Naumann d'Alnoncourt, R.; Thomas, A.; Rosowski, F. Design of an Active and Stable Catalyst for Dry Reforming of Methane *via* Molecular Layer Deposition. *Catal. Today* **2021**, 362, 47–54. <https://doi.org/10.1016/j.cattod.2020.04.050>.
- (54) Sahoo, S. K.; Rao, P. V. C.; Rajeshwer, D.; Krishnamurthy, K. R.; Singh, I. D. Structural Characterization of Coke Deposits on Industrial Spent Paraffin Dehydrogenation Catalysts. *Appl. Catal. A Gen.* **2003**, 244 (2), 311–321. [https://doi.org/10.1016/S0926-860X\(02\)00603-8](https://doi.org/10.1016/S0926-860X(02)00603-8).

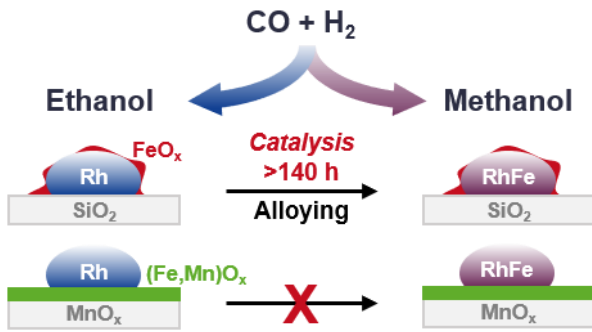


Table of Contents/Abstract Graphic.